Pergamon

Journal of Structural Geology, Vol. 17, No. 10, pp. 1455 to 1472, 1995

0191-8141/95 $9.50 + 0.00

0191-8141(95)00034-8

Mathematical block-motion model for deformation of a layer above a buried fault of arbitrary dip and sense of slip

THOMAS L. PATTON

Amoco, P. O. Box 800, Denver, CO 80201, USA.

and

RAYMOND C. FLETCHER

Department of Geoscience, New Mexico Institute of Mining and Technology, Socorro, NM 87801

(*Received* 13 *October* 1992, *accepted in revised form* 16 *March* 1995

Abstract—An analytic series solution is obtained for the stress and deformation in an isotropic viscous, or incompressible elastic layer subjected to rigid-block motion at its base. The block motion approximates slip on a pre-existing basement fault of arbitrary dip and sense of slip. Deformation in the layer due to horizontally-separating and horizontally-converging blocks, slip on a vertical basement fault, and slip on 45°-dipping reverse and normal basement faults is examined. Above horizontally-diverging and -converging blocks, a symmetric syncline and anticline form, respectively. Monoclines form above dipping basement faults. The location of the monocline, and to a lesser degree its form, vary systematically with fault attitude and sense of slip. For a given fault displacement, the region of brittle failure in a basement normal-fault model is larger than that in a reverse-fault model. New faults formed in the layer are arcuate in profile. Model results agree with observations of stress orientation and deformation from laboratory models.

INTRODUCTION

Mathematical and laboratory models of the deformation of a layer due to dip-slip motion on a basement fault, and of the upward propagation of the fault, have been actively studied since the classic papers of Hafner (1951) and Sanford (1959). The results have been applied to monoclines above vertical (Reches & Johnson 1978) or reverse (Gangi *et al.*, 1977, Rodgers & Rizer 1981) faults.

Models have been formulated in two ways. In most models, an overlying layer is deformed in response to the relative motion of rigid blocks. Such a model is appropriate for a fault which cuts strong basement rock below a sequence of weaker sedimentary rock. This model is conveniently treated in the laboratory, or mathematically. In most experimental models, the basement is simulated by 'forcing blocks' that are effectively rigid, relative to the overlying layer. For example, layers of clay or sand (Fig. 1) are deformed by the relative motion of blocks of steel or wood (e.g. Sandford 1959, Lowell 1970, Horsfield 1977, Stearns *et al.*, 1978, Tsuneishi 1978, Withjack *et al.*, 1990), or rock laminates (Fig. 1b) are deformed above blocks of steel or stronger, unlaminated rock (Stearns & Weinberg 1975, Friedman *et al.*, 1976a, b, 1980, Weinberg 1979, Patton 1984). Horizontal block motion (Figs. 1a & e) has also been used to experimentally model a convergent 'subduction system' (Malavieille 1984, Malavieille *et al.*, 1993), and a divergent 'listric fault system' (Cloos 1968). Many of the mathematical models, starting with that of Sanford (1959), and including that treated here, are also of the block-motion type. The velocity, or displacement, imposed at the base of the layer is precisely equivalent to the relative motion of rigid blocks.

A second type of model is more appropriate if the contrast between the properties of the rock mass cut by the fault and the overlying rocks is minimal, or non-existent. In the mathematical model of Rodgers & Rizer (1981), a distribution of edge dislocations equivalent to slip on a fault, is inserted below the upper surface of a uniform elastic half-space. The only experimental model of this type known to us is the photoelastic thrust-fault model of these authors.

In this paper, we show that a block-motion model for arbitrary fault dip and sense of slip may be constructed from appropriate proportions of two end-member models; one for a vertical fault, the other for a narrow locus of extension or shortening, at which the basement blocks separate or 'interpenetrate', respectively. The normal fault case (Patton 1984) has not been previously reported in the literature.

Although we discuss the models within the context of fault-bound basement blocks beneath an unfaulted section of rock, the block-motion boundary conditions are applicable to other kinds of tectonic deformation as well. For example, separating rigid blocks may be used to simulate boudinage structure, where the solutions apply to the deformation of material above the boudin gaps. The block motion may instead be an interpenetration, corresponding to dissolution along a solution seam confined to a stiff layer.

A brief comparison is made between the embedded crack and the block-motion models for the case of an

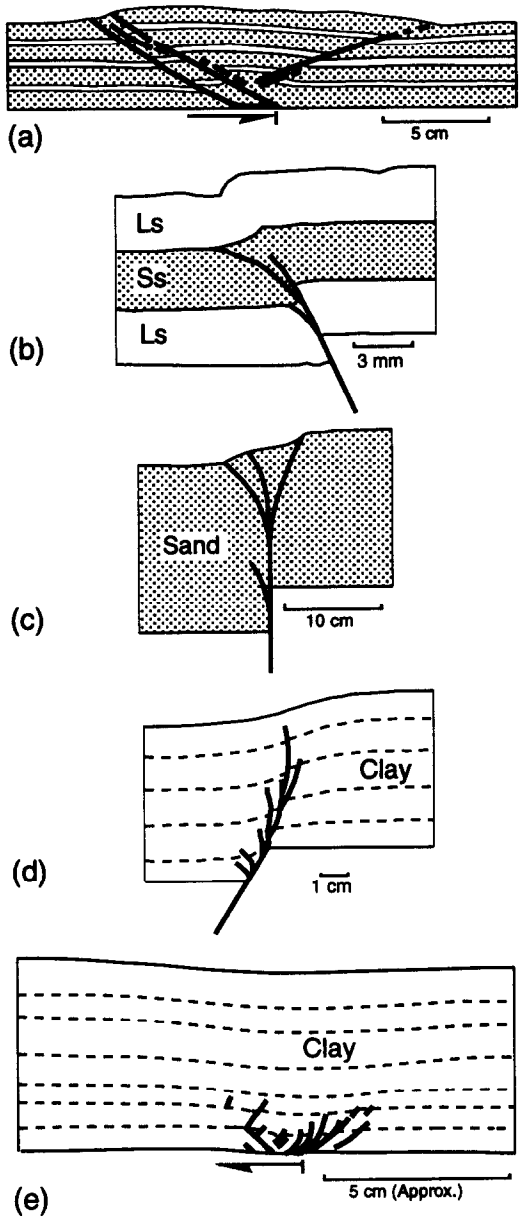

Fig. 1. Laboratory models showing deformation associated with rigid-block-motion boundary conditions. (a) A horizontal 'conveyor belt' fault system, modeling a subduction complex beneath sand and clay layers (Malavieille 1984). (b) A 60°-dipping reverse, basement fault deforming limestone (Ls) and sandstone (Ss) rock beams at 100 MPa confining pressure (Friedman *et al.*, 1976a). (c) A vertical basement fault beneath unconsolidated sand (Stearns *et al.*, 1978). (d) A 60°-dipping normal fault beneath a clay cake (Withjack *et al.*, 1990). (c) A horizontal 'conveyor belt' extensional fault deforming a clay cake (Cloos 1968).

overlying half-space. We then illustrate the deformation of a layer by means of a deformed grid. The stress distribution is used to estimate the form of a region of failure within the layer, and the orientation of faults within it. Lastly, we compare the mathematically-derived results with observations from laboratory models and natural examples.

MODEL AND ANALYSIS

Because of the formal correspondence between solutions for elastic and viscous bodies, the layer may be considered to be either, but the results obtained here apply only to an incompressible medium. For an elastic layer, the amount of slip on the fault, U, is specified, and stress and *displacement* fields in the layer are obtained. The stress in the layer associated with fault slip will scale with GU/H, where G is the elastic shear modulus, and H is the layer thickness. In the case of a viscous layer, the slip rate V is specified, and stress and *velocity* fields are obtained. The stress scales with $\eta V/H$, where η is the layer viscosity. For definiteness, we keep to the choice of the viscous layer. The layer is isotropic.

The analysis differs only in detail from that given in Sanford (1959). The layer is welded to a series of rigid blocks of width $L/2$ (Fig. 2). Blocks are separated by faults, all of which dip in the same direction, and the sense of slip alternates. Accordingly, the solution obtained is periodic in the horizontal coordinate x, and models alternating normal and reverse faults with the same dip, δ. In order for the faults to be effectively isolated, $L/H \gg 1$; in the computed results, $L/H = 16$. A motion with length-scale L, corresponding to flow from loci of block interpenetration to adjacent loci of block separation, will always be present.

The motion of the fault blocks to either side of a fault over one wavelength of the periodic motion is given by

$$u(x,0) = \begin{cases} -V\cos\delta & -L/2 \le x \le 0 \\ +V\cos\delta & 0 \le x \le L/2 \end{cases} \quad (1a)$$

$$w(x,0) = \begin{cases} -V\sin\delta & -L/2 \le x \le 0 \\ +V\sin\delta & 0 \le x \le L/2 \end{cases} \quad (1b)$$

The upper surface of the layer is traction-free. In the present solution it is taken to be planar. The boundary conditions there are

$$\sigma_{xz}(x,H) = 0$$
$$\sigma_{zz}(x,H) = 0 \quad (2)$$

If appreciable topography were established by the deformation, it would contribute normal loads at the upper surface proportional to the stabilizing density contrast there. If the layer is elastic, the relief due to the displacement at the surface will be negligible for any reasonable value of fault displacement. On the other hand, relatively large relief could be accumulated by deformation of a viscous layer. This is not accounted for in the solutions obtained, although it would be easy enough to do so. Hence, we suppose either that the deformation has not progressed to the point where the surface relief has become appreciable, or that erosion and deposition have maintained a nearly planar upper surface.

Because the relation between stress and rate of deformation is linear, the solution for the boundary conditions (1) and (2) can be separated into two independent, additive parts, one for horizontal relative motion of the rigid blocks, and one for vertical motion. Horizontal motion corresponds to a fault of zero dip, or to a narrow locus of block separation or interpenetration. The velocity boundary conditions for the horizontal motion is obtained by augmenting condition (1a) with

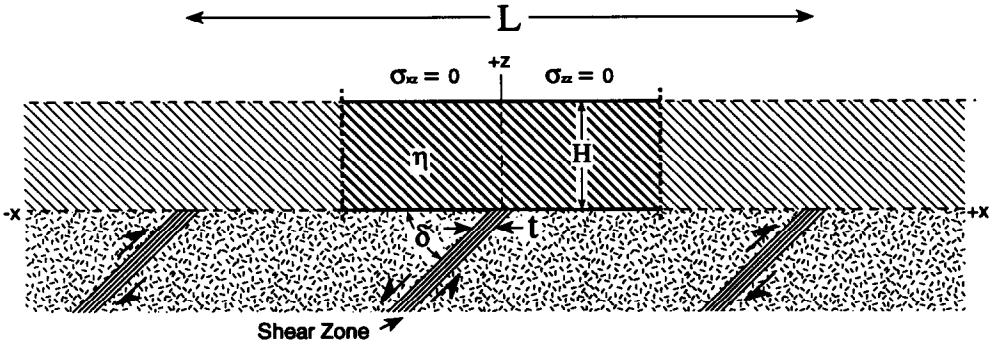

Fig. 2. Boundary conditions for the block-motion model. The layer (cross-hatching) extends to infinity in the $+x$ and $-x$ directions, and has viscosity η and thickness H. The upper surface is stress free ($\sigma_{zz} = \sigma_{xz} = 0$) and the lower surface is subjected to periodically repeating (at intervals of L/2 where L is the wavelength) faults with constant dip (δ) but alternating sense of slip. The thickness of the shear zone associated with the fault is 't'. Block-motion model results for individual faults derive from the mathematical isolation of a segment of the layer (dark, cross-hatching) of length $\leq L/2$. Block-motion models presented in this manuscript have isolated the region $-L/8 \leq x \leq L/8$ for analysis and used a layer/thickness ratio (L/H) of 16 to minimize the effects of the adjacent faults.

$$w(x,0) = 0, \qquad -L/2 \leq x \leq L/2 \tag{3a}$$

and those for the vertical motion by augmenting the condition (1b) with

$$u(x,0) = 0, \qquad -L/2 \leq x \leq L/2 \tag{3b}$$

This decomposition is useful in that we can think of the velocity or stress distribution associated with a fault of any dip and sense as the additive sum of these two parts.

The solutions for the layer velocities and stresses for each of the component block motions, in turn, are series solutions in elementary sinusoidal solutions (Sanford 1959, Couples 1977, Reches & Johnson 1978). These are given in the Appendix. In the numerical evaluation, the series are truncated at N terms and, hence, the results apply rather to narrow shear zones of width $t \approx L/2N$, or, since $L = 16H$, $t \approx 8H/N$.

In the laboratory models cited in Fig. 1, no provision is made for a 'regional stress'; the deforming media are not subjected to a 'push' or 'pull' at the ends. The stress distribution arises solely from the relative motion of the underlying blocks or inextensible sheets, and the stress dies off away from the locus of interaction of the two blocks. Likewise, our block-motion model ignores the contribution of regional stress relative to that arising from the motions of the blocks. In the mathematical model, a regional stress may be introduced, if desired. This is allowed, because the rheological behavior adopted is a linear one. An explicit picture of the addition of regional stress is as follows. Let the layer be subject to the regional stress, in which case it will contract or stretch horizontally. Now bond the layer to the rigid blocks or inextensible sheets, and apply the prescribed motions to these. In the present case, we have not explored the effects of adding such a regional stress, but our supposition is that the stresses arising from the relative motion of the basement blocks will predominate in many natural cases. Others may use the present solution, or a similar one, to explore the alternative possibility.

RESULTS

Comparison of half-space, block-motion models with crack tip models

It is instructive to compare the two types of models described in the introduction for the simpler case of a half-space. The velocity and stress distributions for purely horizontal block motion are compared with the near-tip velocity and stress distributions for a vertical mode I crack. Those for purely vertical block motion are compared with the near-tip quantities for a vertical mode II crack.

Excluding the absolute magnitudes of quantities, the near-tip crack fields are scale-independent, while the spatial variation of quantities for the block-motion depends on the size of the region relative to the wavelength L. Large-scale features become apparent for regions with dimension larger than about $L/6$. To relate results for the half-space to those for the layer, in which $H = L/16$, it is useful to scale an appropriate stress quantity for the crack and block-motion models so that it is equal at the point $(0, L/32)$, above the fault at half the thickness of the 'layer'.

The velocity field is conveniently illustrated by contours of the stream function. The velocity vector at any point is tangent to a streamline, and its magnitude is inversely proportional to the spacing between them. The periodic horizontal block motions give rise to circulation in the half-space between loci of extension and shortening. Over the square with base $-L/4 \leq x \leq L/4$, the circulation is evident (Fig. 3a). The near-tip approximation for a mode I crack is similar only within a region near the locus of extension, as shown by plotting its stream function (Fig. 3b), using the same number of contours. The magnitude of flow driven by the block motion dies off upwards; in the near-tip approximation for the crack, the velocity *increases* away from the tip as $\sqrt{r}$, consistent with the $\sqrt{(1/r)}$ die-off in stress. The streamlines clearly indicate block motion by their strict

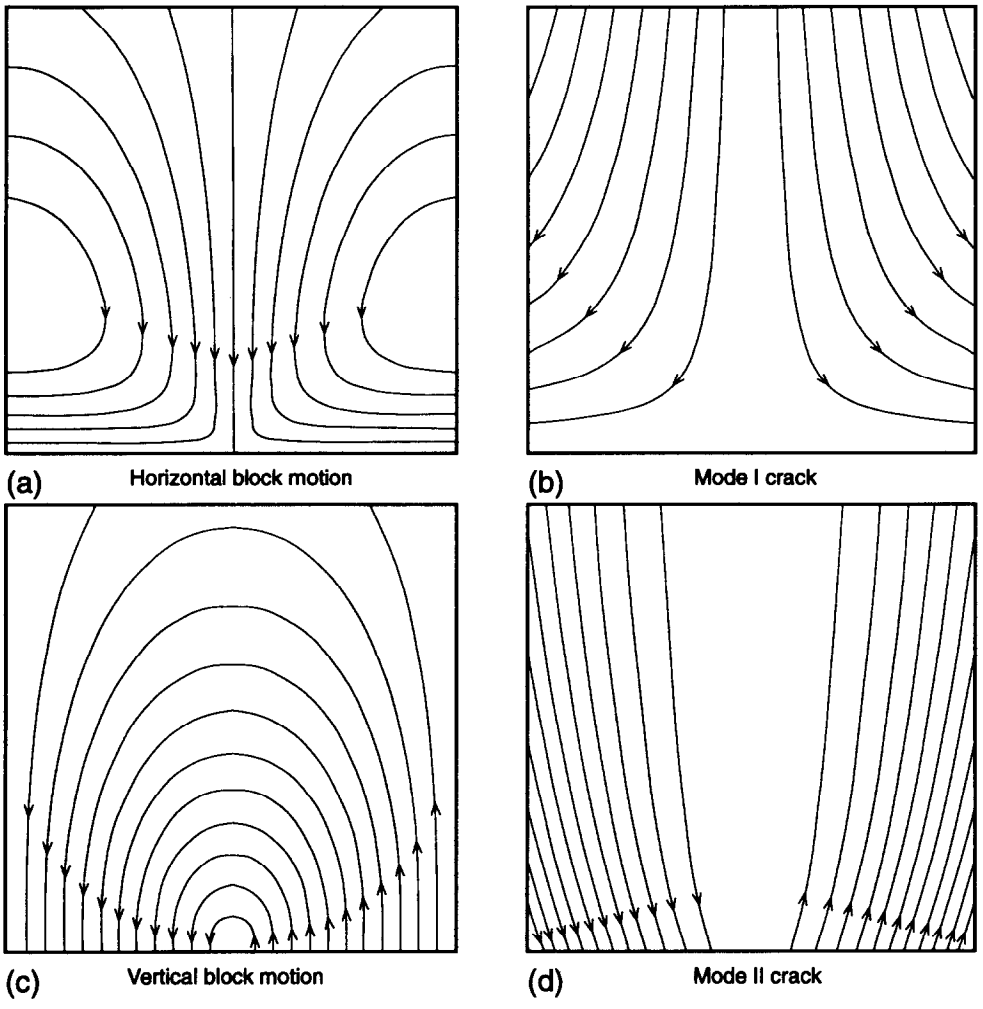

Fig. 3. Comparison of stream functions among infinite half-space block-motion models and mode I and mode II crack models. Contours of the stream function for divergent, horizontal block motion (a), in the square region with base $-L/4 \leq x \leq L/4$. The large-scale flow between loci of block separation is clearly seen; the surfaces $x = \pm L/4$ are mirror planes for the *form* of the streamlines, excluding the flow direction. For 'interpenetration' or convergence the form of the contours remains the same, but the direction of flow reverses. Contours of the stream function for flow near the tip of an opening mode I crack (b); for better definition, a few more contours are used than in (a). Contours of the stream function for vertical block motion (c), in the region $-L/4 \leq x \leq L/4$. Contours of the stream function for a vertical mode II crack (d), near-tip approximation. The same number of contours is used as in (c).

parallelism with the block surface near it. The streamlines for the purely vertical block-motion (Fig. 3c) differ in several respects from those for the vertical mode II crack (Fig. 3d). Again, the block motion at the base is evident from the precisely vertical and evenly-spaced streamlines there, and the circulation in the block-motion is indicated by the horizontal attitudes of streamlines above the fault. The jump in velocity along the mode II crack goes to zero at its tip, and increases away from the tip. The contrast between rigid blocks and the deformable medium below the horizontal plane passing through the crack tip is indicated by motion away from the crack on the 'up-thrown' side, and towards it on the 'down-thrown' side.

Stream functions for block motions along dipping faults may be obtained by adding those for the horizontal and vertical motions in suitable proportions. Figure 4 shows the result for a 45° west-dipping normal fault. The reverse fault model is distinguished only by a change in direction of motion along the streamlines. The crack models do not superpose in the same manner; a vertical, mixed mode I and II crack is not equivalent to a dipping mode II crack.

In comparing stresses for an horizontal block motion with those for a vertical, mode I crack, we scale the mean stresses for each so that they equal unity at the point (0, $L/32$). The region of observation will be taken as the square with side $L/8$; twice this horizontal span is used in the figures of the layer models. The coordinates used on these figures are in multiples of the 'layer thickness', or $L/16$. An unconventional choice of contours that differ by factors of two conveniently shows the dependence on distance from the fault tip. Forty-one terms were kept in the series expansions for the block-motion quantities. Close to the fault, the local behavior is that for a 'shear zone'; the short-wavelength terms have no effect away from it.

For the mean stress, the *vertical* dependence away from the fault in the block-motion model (Fig. 5a) is $\sim 1/r$; and the fully *radial* dependence for the crack model

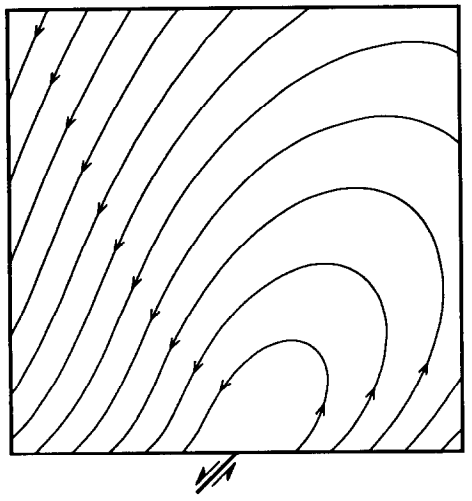

Fig. 4. Contours of the stream function in the block-motion model for a 45° west-dipping normal fault, obtained by summing the stream functions resulting from equal contributions of vertical (Fig. 3a) and horizontal (Fig. 3c) block motions.

(Fig. 5b) is $\sqrt{(1/r)}$. The effect of the rigid blocks is to cause the mean stress to drop to zero at the block surfaces, except in the shear zone. In the maximum shear stress distributions for the two models (Figs. 5c–d), the block-motion model demonstrates a somewhat larger region of higher shear stress around the fault tip.

In the results for vertical block motion and a vertical mode II crack (Fig. 6) the maximum shear stress is used to normalize the stress quantities. For the mean stress (Figs. 6a–b), the same features discussed in the comparison of the previous pair of models are duplicated here. For block motion, the contours of shear stress (Fig. 6c) converge towards the fault tip, since the deviatoric stress is zero at the block surfaces. As more terms are retained in the series, the location of the maximum migrates towards the fault tip, and its magnitude increases, without bound. In contrast, the maximum shear stress for the mode II crack (Fig. 6d) does not vanish along the horizontal plane corresponding to the base of the layer in the block-motion model.

Overall, this comparison suggests that estimates of deformation above a buried fault from block-motion or crack models will be similar.

Layer, block-motion models

Deformation. A deformed, initially square grid is most useful in the comparison between the mathematically-modeled deformation and that observed in laboratory models and natural examples. The deformed grid is obtained by computing the velocity at each initial grid point, multiplying it by a time increment, and advancing the particle to the new position.

Although the solution is for a flat upper surface, we retain the entire deformed grid for clarity. We choose the time increment to give a fault displacement equal to 0.2 the layer thickness. Although we refer to the subhorizontal lines as 'bedding', we do not imply that the layer is anisotropic. We refer to the left- and right-hand sides of the models as west and east, respectively. Throughout the discussion, we refer to the narrow zone between blocks as the location of the 'basement fault'.

In horizontal block-convergence, a symmetric, upward-widening, anticline forms above the basement fault (Fig. 7a). Near the fault, initially square grid elements are shortened parallel to bedding. In horizontal block divergence, grid elements near the fault are elongated parallel to bedding, resulting in a symmetric, upward-widening syncline in the layer (Fig. 7e). Vertical block-motion results in an upward-widening monocline. The neutral point of the monocline, at which the vertical displacement is zero, is centered above the basement fault (Fig. 7c). Grid elements in the upthrown portion of the layer show bedding-parallel elongation; those in the down-thrown portion show bedding-parallel shortening.

Summing the velocities for the vertical and horizontal block motions in suitable proportions, yields the deformed grids for reverse or normal faults (Figs. 7b & d). Slip along a basement normal fault with 45° dip generates a broad monocline (Fig. 7d). The lower hinge of the monocline is complicated by the presence of a low-amplitude syncline. With increased dip on the basement normal fault, the amplitude of the syncline is reduced and its trough migrates west. The neutral point of the monocline lies to the east of the basement fault. The monocline associated with a basement reverse fault with 45° dip (Fig. 7b) has an anticline superposed on its upper hinge. With increasing fault dip, the amplitude of the anticline decreases and its crest migrates towards the east, away from the basement-fault location. The neutral point of the monocline lies to the west of the basement fault.

Stress distribution. The stresses described here are those due to the block motion alone, and exclude the lithostatic and any 'regional' contributions. Horizontal block convergence generates a lobe of compressive (negative) mean stress above the tip of the basement fault (Fig. 8a). The lobe is flanked by two regions of low tensile (positive) mean stress. The mean stress decreases upward in the layer. Horizontal block divergence produces a mean stress distribution (Fig. 8e) identical in form to that of the convergence model, but everywhere of opposite sign. The mean stress distribution for the vertical block-motion model (Fig. 8c) has a central line of symmetry across which the sign changes. A region of large gradient in mean stress above the basement fault separates a region of tensile mean stress on the down-thrown side of the layer from a region of compressive mean stress on the upthrown side. In the upper portion of the layer, the positions of regions of tensile and compressive mean stress are reversed.

The value of a stress component for a dipping fault model is obtained by adding the values obtained from the horizontal and vertical block-motion solutions, in suitable proportion. Thus, the mean stress, which is one-third the sum of the three normal stress components, is also additive. For a basement normal fault with 45° dip (Fig. 8d), a region of large tensile mean stress immedi-

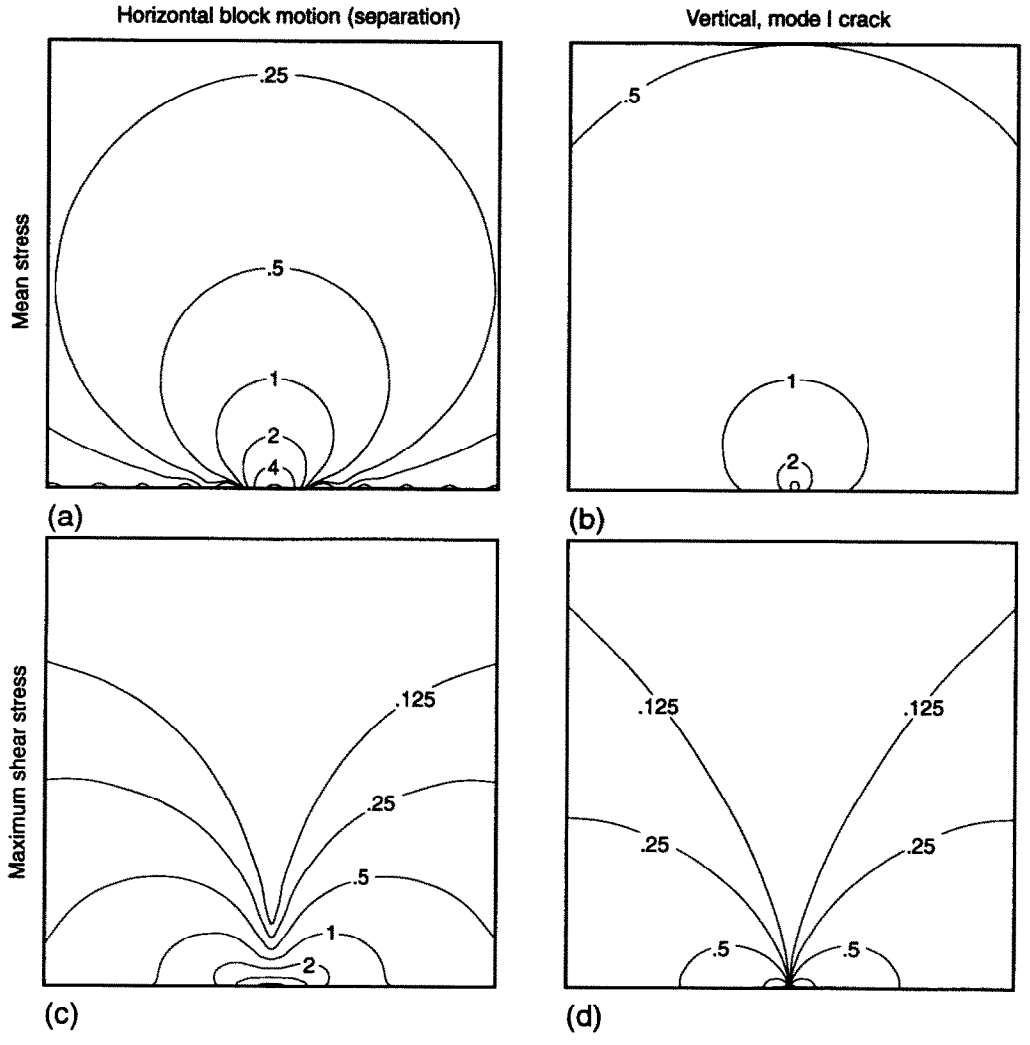

Fig. 5. Comparison of mean stress and maximum shear stress distributions for the infinite half-space, horizontal block-motion model and the vertical, mode I crack model. Contours of mean stress for (a) horizontal block-motion (separation) in the square region with base $-L/16 \leq x \leq L/16$, or $-H \leq x \leq H$, where H is the 'layer thickness' (see text). The mean stress is normalized so as to equal unity at the point $(0, H/2)$. Contours of mean stress (b) for the near-tip field of an opening, vertical mode I crack, normalized to equal unity at $(0, H/2)$. Contours of maximum shear stress (radius of Mohr's circle) for horizontal, divergent block motion (c). Stress normalization is consistent with that in (a). Contours of maximum shear stress (d) for the near-tip field of an opening, vertical mode I crack. Normalization is consistent with that in (b). In each diagram, sequential pairs of contours differ by a factor of 2 ($-8, -4, -2, -1, -1/2, -1/4, -1/8, 0, 1/8, 1/4, 1/2, 1, 2, 4, 8$). Contours are in units of $\eta V/H$ or GU/H.

ately overlies the basement-fault, with an adjacent region of weaker compressive mean stress at the base of the layer to the east. In contrast to the vertical basement-fault model, where the large gradient in mean stress directly overlies the fault, the large mean-stress gradient in this model lies to the east of the basement-fault location. The region of tensile mean stress extends obliquely across the layer, dominating the eastern half of its upper portion. A small region of compressive mean stress lies to the west of the center of the layer near its upper surface. The form of the contours for the mean-stress distribution above a basement reverse fault with the same dip and dip direction (Fig. 8b) is identical to that for the basement normal fault model, but with a change in sign.

Contours of maximum shear stress $\sqrt{J_2} = [1/4(\sigma_{xx} - \sigma_{zz})^2 + \sigma_{xz}{}^2]^{1/2}$, for the vertical block-motion model (Fig. 9c) and the horizontal convergent (Fig. 9a) and divergent (Fig. 9e) block-motion models, are symmetrically distributed about a vertical line above the basement-fault location. The maximum shear stress distributions for the two horizontal block-motion models are identical. A wide region of large shear stress is located above the basement fault. Upward, the single region of high shear stress separates into two lobes which angle across the layer to its upper surface. The shear-stress gradient above the basement-fault location is large, resulting in low shear stress in the central portion of the layer. For the vertical block-motion model, high values of maximum shear stress are present in the central portion of the layer, above the basement-fault location. At the base of the layer, the region of high shear stress is narrow, with large gradients adjacent to the basement-fault location. In both the horizontal and vertical block-motion

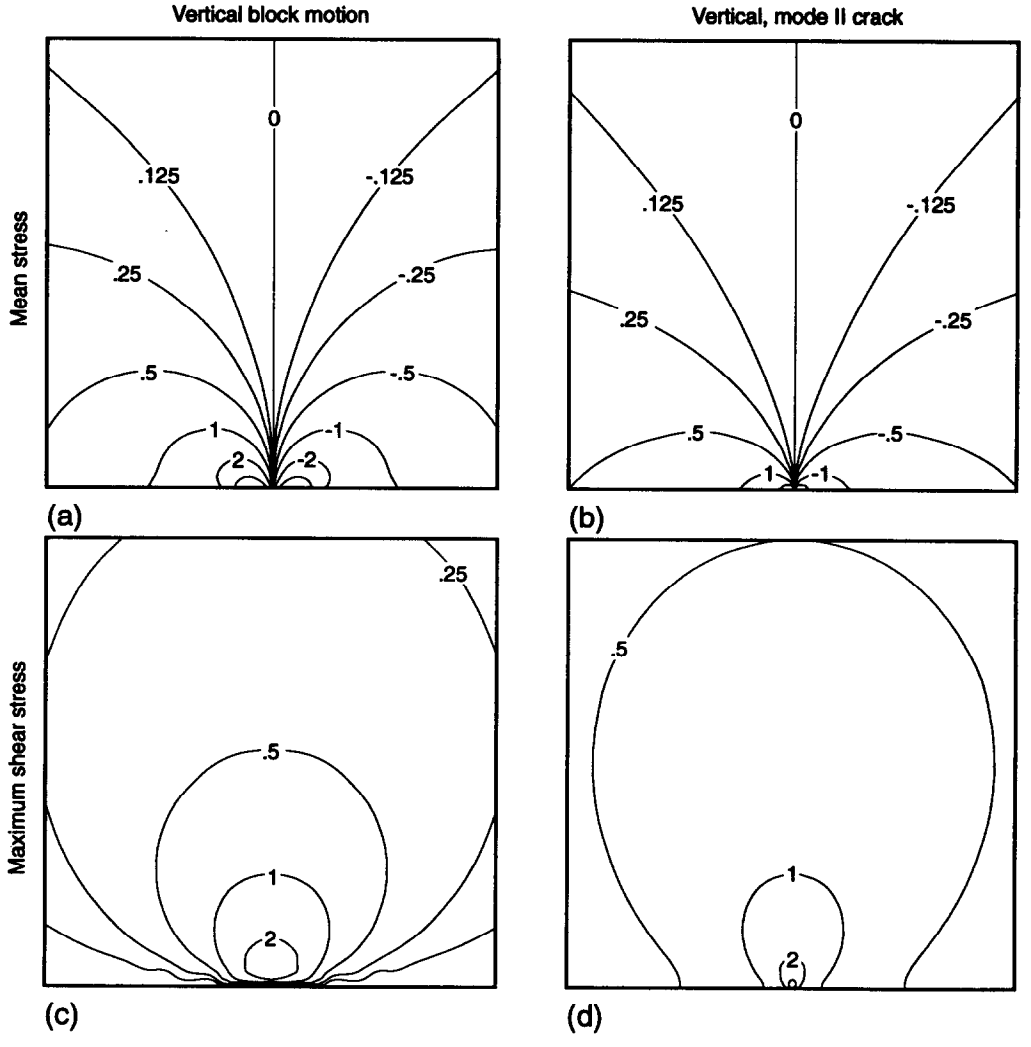

Fig. 6. Comparison of mean stress and maximum shear stress distributions for the infinite half-space, vertical block-motion model and the vertical, mode II crack model. Contours of mean stress (a) for vertical block motion. Above the upthrown block, the mean stress is negative (compressive). Contours of mean stress (b) for the near-tip field of a vertical, mode II crack. Contours of maximum shear stress (c) for vertical block-motion. Contours of maximum shear stress (d) for the near-tip field of a vertical mode II crack. Contours of both mean stress and maximum shear stress are normalized relative to the maximum shear stress equaling unity at the point (0, $H/2$). Contours are in units of $\eta V/H$ or GU/H.

models, the central, upper portion of the layer has lower shear stress values, flanked by slightly higher shear stress to the east and west.

To obtain maximum shear stress distributions for dipping basement-fault models, we must first calculate the individual stress components for the vertical and horizontal solutions, add them in suitable proportions, and then form the quantity $\sqrt{J_2}$. The basement normal-fault model (Fig. 9d) shows a lobe of high shear stress extending from the basement fault obliquely across the layer to its upper surface. The hint of a second lobe, similar to that seen in the horizontal block-motion models, lies to the west of the fault location. A significantly wider region of high shear stress is present at the base than in the case of the vertical block-motion model. The maximum shear-stress distribution for the basement reverse fault (Fig. 9b) is identical to that of the normal fault when viewed such that both faults have the same dip direction.

Maximum compressive stress orientation is generally horizontal to moderately inclined for the horizontal, convergent block-motion model (Fig. 10a) and moderately inclined to vertical for the horizontal, divergent block-motion model (Fig. 10e). For the vertical block-motion model (Fig. 10c), maximum compressive stress orientation in the eastern half of the layer is similar to that of the horizontal divergent block-motion model, and that in the western half of the layer is similar to that of the horizontal convergent block-motion model. For the basement normal-fault model (Fig. 10d), the maximum principal stress orientation is similar to that for the horizontal, divergent block-motion model in regions away from the basement fault location. The orientation in the region above the basement fault is similar to that above the fault in the vertical block-motion model. Along the upper portion of the layer, the maximum compressive stress is horizontal in a limited area immediately to the west of the basement fault. It is vertical in adjacent regions. The orientation of the maximum compressive stress in the basement reverse-fault model (Fig. 10a) is similar to that in the horizontal, convergent block-motion model in regions away from the fault, and

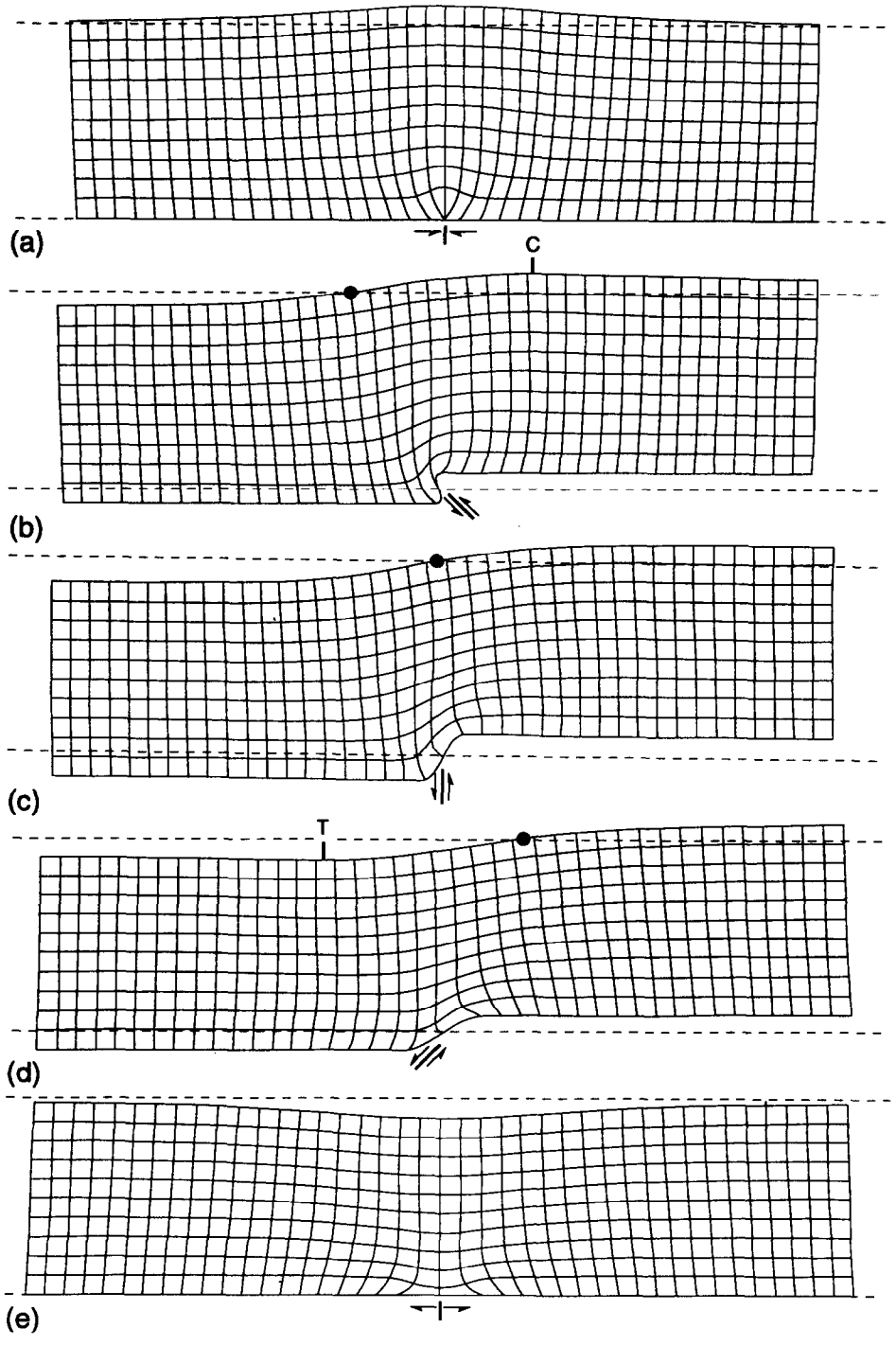

Fig. 7. Deformation of initially equant grids associated with layer, block-motion models for a: (a) convergent, horizontal fault; (b) reverse fault with 45° dip; (c) vertical fault; (d) normal fault with 45° dip; and (e) divergent, horizontal fault. The velocity, and the resulting flow portrayed by the deformed grid, has been exaggerated to allow comparison among models. The horizontal dashed lines represent the original, undeformed layer position and thickness. 'C' identifies the crest of a hanging wall anticline; 'T' identifies the trough of a hanging wall syncline. Neutral points (loci of no apparent vertical motion) at the upper surface of the layer are identified with solid dots.

similar to that in the vertical block-motion model in the region above the tip of the basement fault. Again, the maximum compressive stress orientation near the upper surface of the layer is vertical within a limited region lying immediately to the east of the basement fault, and horizontal in adjacent regions.

The stress distributions obtained in these models are closely similar to those obtained from mathematical models for reverse faults (e.g. Gangi *et al.*, 1977, Rodgers & Rizer 1981) and vertical faults (e.g. Sanford 1959, Haneberg 1992, 1993) that use similar boundary conditions.

Brittle failure. One goal of modeling is the mechanical rationalization of observed natural or experimental discontinuous structures, which form predominantly by

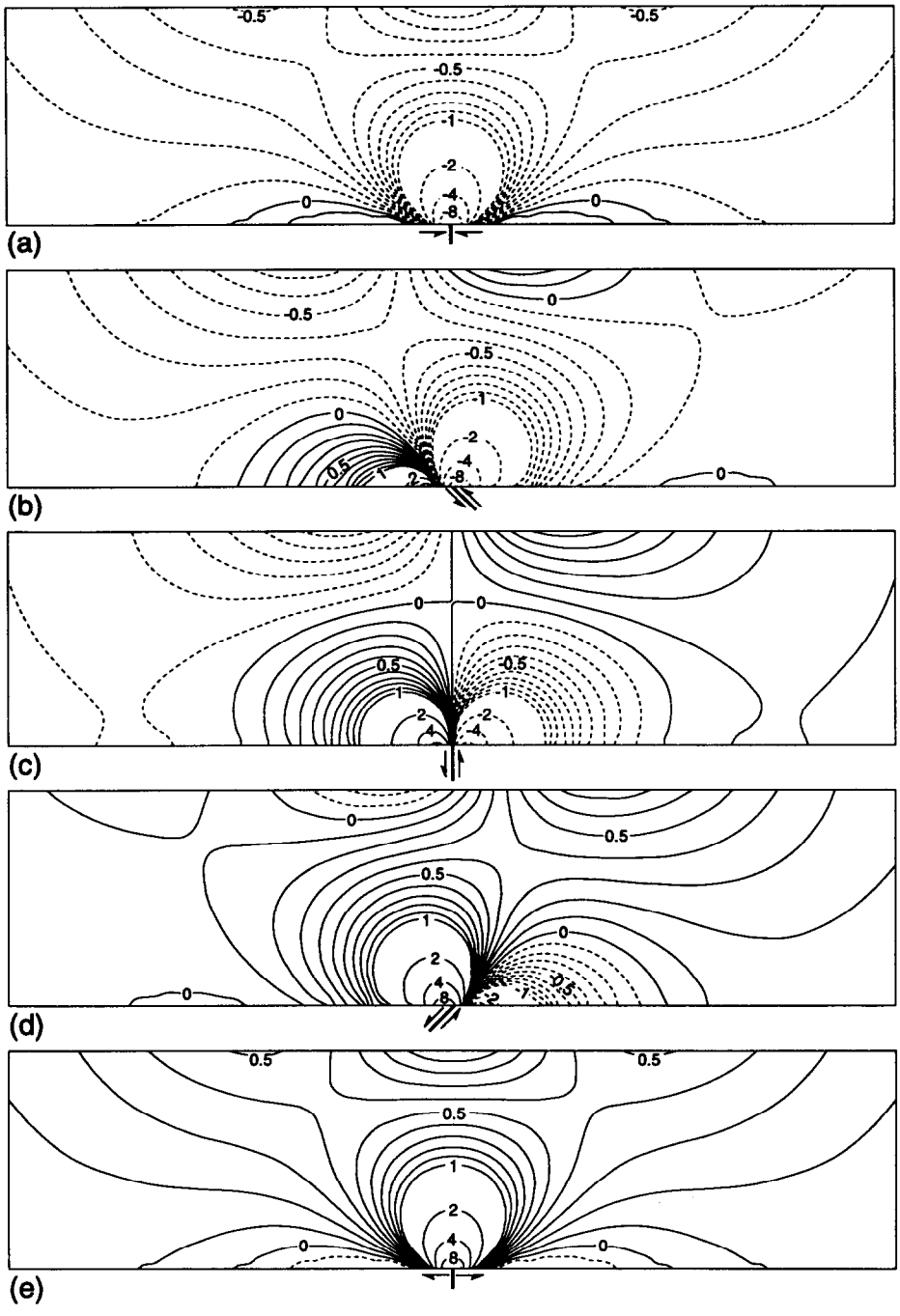

Fig. 8. Contours of dimensionless mean stress associated with the layer, block-motion models of a: (a) convergent, horizontal fault; (b) reverse fault with 45° dip; (c) vertical fault; (d) normal fault with 45° dip; and (e) divergent, horizontal fault. Compression is negative and tension is positive. Contours >1 and <-1 increase by a factor of 2 for each subsequent contour (e.g. 1, 2, 4, 8). Contours between -1 and 1, have a contour interval of 0.1. Contours are in units of $\eta V/H$ or GU/H.

brittle behavior: micro-cracking, crystal-plastic deformation, jointing, faulting, and the propagation of the underlying fault zone.

It has been customary to use stress distributions, such as those obtained here, to make estimates of the distribution, nature, and evolution of brittle deformation (Hafner 1951, Sanford 1959, Howard 1966, Couples 1978). This procedure is not rigorous, beyond determining the first point of failure, since, once failure begins, the body no longer behaves as an elastic or viscous body, or as the same elastic or viscous body. For example, a fault can be treated as a discrete cut on which certain conditions are met, but the stress distribution in the new, faulted body is no longer that in the unfaulted body. The rough agreement between results obtained this way and observations from experimentally or naturally deformed structures, however, supports the use of the method as a convenient first approximation.

The model stress distribution may be used to infer the onset, distribution and nature of brittle failure, by faulting, in the layer. The procedure used is that of Kilsdonk & Fletcher (1989), with a modification to include the effect of lithostatic stress.

The dimensionless failure criterion, $f^* = 0$, is given by

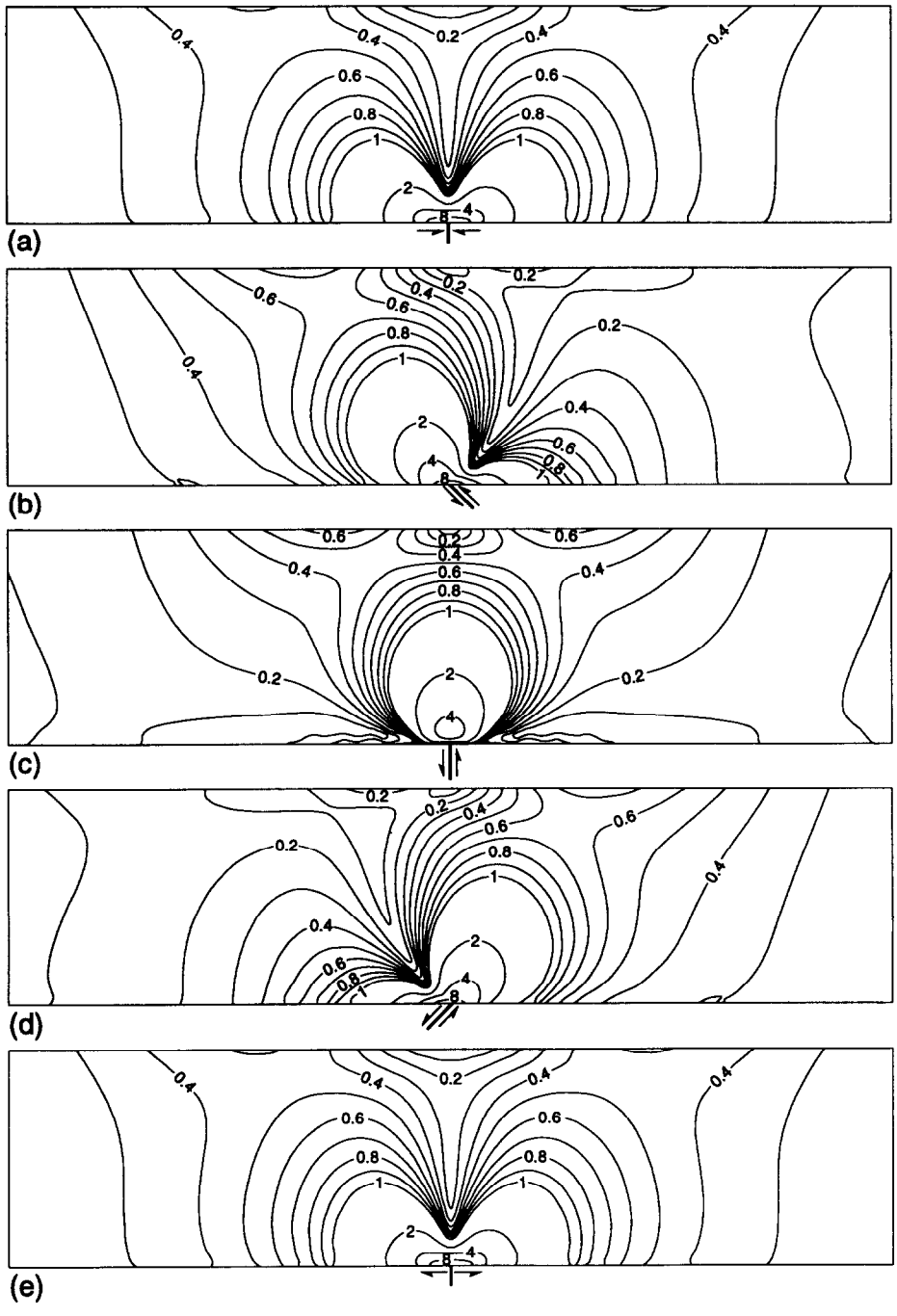

Fig. 9. Contours of dimensionless deviatoric stress ($\sqrt{J_2}$) associated with the layer block-motion models of a: (a) convergent, horizontal fault; (b) reverse fault with 45° dip; (c) vertical fault; (d) normal fault with 45° dip; and (e) divergent, horizontal fault. Contours >1 and <−1 increase by a factor of 2 for each subsequent contour (e.g. 1, 2, 4, 8). Contours between −1 and 1, have a contour interval of 0.1. Contours are in units of $\eta V/H$ or GU/H.

$$f^* = \tau^* - \tau_c^* + \sin\phi[\sigma^* + \alpha(z/H - 1)] = 0 \quad (4)$$

where $\tau^* = \tau/[2\eta V/H]$ is a dimensionless maximum shear stress, and $\sigma^* = \sigma/[2\eta V/H]$ is a dimensionless mean stress, and

$$\tau_c^* = \tau_c H/(2\eta V) \quad (5a)$$

$$\alpha = \rho g H^2/(2\eta V) \quad (5b)$$

where τ_c is the cohesion.

By adopting as the basic rheological behavior that of a viscous fluid, we have opted for creeping flow as the dominant response of the layer. Most other modelers of deformation above basement faults (e.g. Sanford 1959, Rodgers & Rizer 1980) adopt elastic behavior. The only real significance of our choice is that the material be restricted to be incompressible. We can switch the behavior of the layer from viscous fluid to elastic solid at will, by replacing the product ηV by GU. Hence, in evaluating the dimensionless constants above, the reader may choose either. For example, the choice $G = 10^4$MPa, $U = 1$m yields a value of the product $GU = 10^{10}$kg/s^2, as does likewise the product $\eta = \pi \times 10^{19}$ Pa, s and $V = 1$ cm/$a \simeq \pi \times 10^{-10}$m/s. Using $\rho = 2500$ kg/m^3, g = 10 m/s^2, $H = 3$ km, and $\tau_c = 10$MPa, we obtain, in

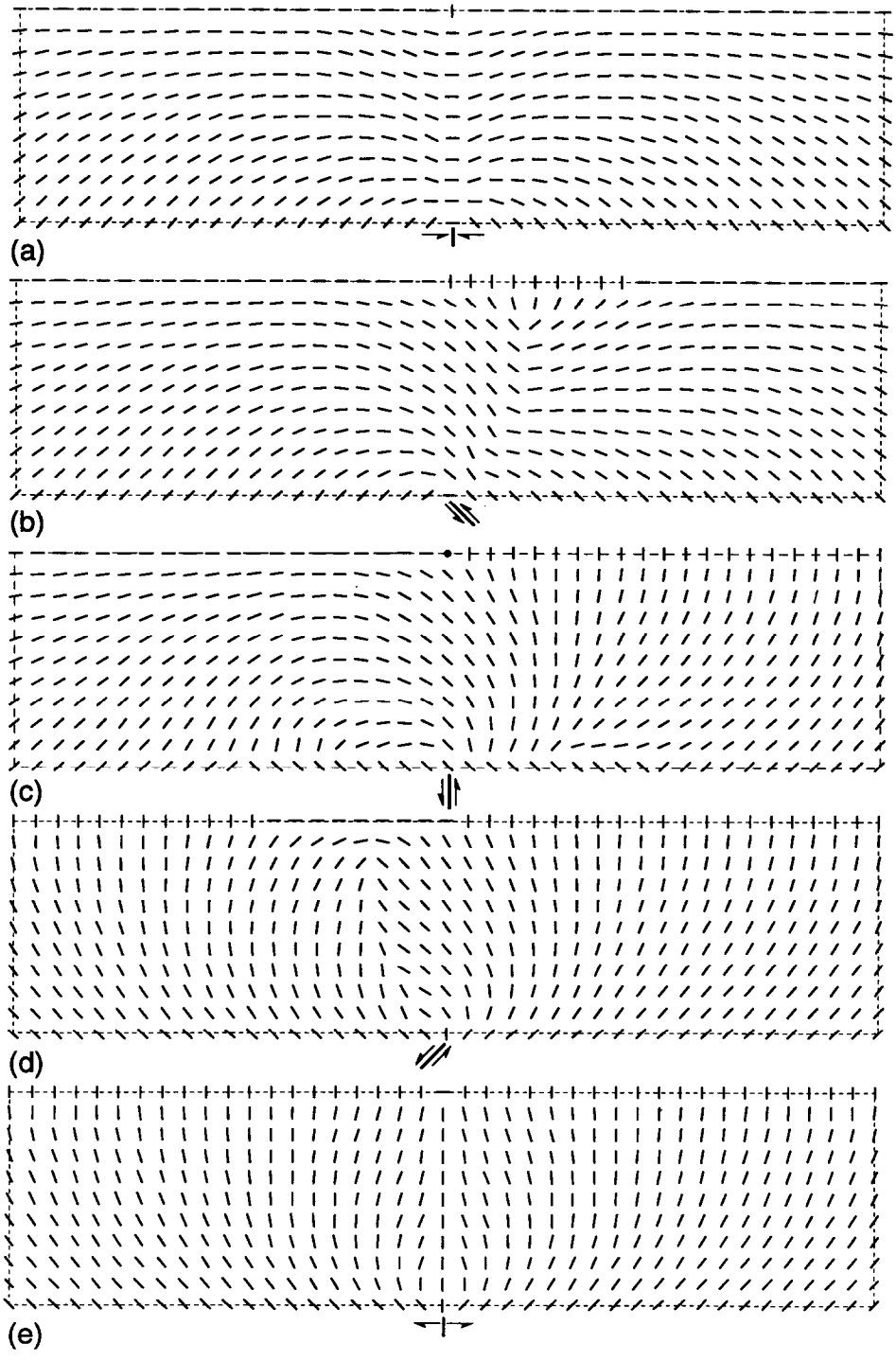

Fig. 10. Maximum compressive stress trajectories associated with layer, block-motion models of a: (a) convergent, horizontal fault; (b) reverse fault with 45° dip; (c) vertical fault; (d) normal fault with 45° dip; and (e) divergent, horizontal fault. Positive isotropic points in the upper portion of the layer are indicated by converging stress trajectories immediately to the east and west of the center of the layer for the reverse- (b) and normal-fault (d) models respectively.

either case, $\tau_c^* = 1.5$ and $\alpha = 11.25$. The value of α is rather large, indicating the dominance of the lithostatic stress relative to the stresses arising from fault motion, except in the immediate vicinity of the fault. Thus, we may anticipate that, for this choice of parameters, the locus $f^* = 0$ will enclose only a small region near the fault, external to which the stresses will fall below the yield condition, $f^* < 0$. An increase in the product ηV or GU by a factor of 10 to 100 leads to more interesting 'regions of failure'.

Notice that, for fixed values of τ_c and ρgH, the two dimensionless groups τ_c^* and α will maintain the same ratio as the product varies. This suggests the following scheme, which is more readily associated with an elastic layer. Let all physical parameters be fixed with the values cited above, yielding a τ_c^*/α ratio of 0.13. Then, as U is increased, the parameters will fall, and, at some point, initial failure will occur. In the present case, initial failure will always occur at the fault zone, provided that it is sharp enough. We may then increase the fault

displacement, U, beyond the point of initial failure, and use the evolving position of the locus $f^* = 0$ to estimate the growing region of failure, until, for example, it finally crosses the entire layer. This procedure clearly pushes at the limits of the approximation, but the result is appealing. If one adopts, instead, viscous behavior, the region of failure is an estimate of the region in which faulting takes place in addition to deformation by mechanisms such as pressure solutuion.

The procedure is carried out for each block-motion model using 111 terms in the series expansions, so, for the above choice of physical parameters, the width of the fault zone is roughly $8H/111$, or, for $H = 3$ km, 216 m. For each block-motion model, the sequence of initial failure ($f^* = 0$) loci, corresponding to increments in displacement of 1 meter on the fault, are drawn (Fig. 11). The displacement on the fault is increased until the loci of failure join to cross the entire layer.

For the horizontal convergent (Fig. 11a) and divergent (Fig. 11e) block-motion models, the regions of failure are symmetric and 'conjugate', leaving an unfailed block between them. The region of failure crosses the entire layer at $U = 10$ m in the convergent model, twice that for the divergent model. The overall orientations of the regions of failure near the basement fault are horizontal, but become steeply inclined higher in the layer with additional fault displacement. For the vertical fault (Fig. 11c), a single throughgoing, asymmetric zone of failure is established at $U = 5$m. The orientation of the region of failure for smaller basement-fault displacement remains nearly vertical throughout much of the layer. For basement-fault displacement less than that for which the failure region crosses the layer, all three models show regions of failure near the upper surface of the layer which are isolated from that above the basement fault.

In the basement reverse-fault model (Fig. 11b), the initial region of failure at the base of the layer is elongated in a direction roughly parallel to the dip of the basement fault. A separate shallow region of failure occurs at the upper surface, to the east of the basement fault. With larger basement-fault displacement, two distinct, vertically elongated lobes of failure form to the west and east of the basement-fault location. The one on the east links with the failure region near the upper surface at $U = 6$ m.

The shape of the failure region above the basement normal fault (Fig. 11d) is more symmetric than that of the basement reverse fault. Through-going failure of the layer occurs at a smaller basement-fault displacement (4 m) for this model than for any of the other basement-fault models.

As in other mathematical models addressing brittle failure, we have assumed that at every point within the region of failure, two fault orientations ('X' in Fig. 11) are possible at an angle of 30° to either side of the maximum compressive stress. By this relationship, our models describe arcuate rather than planar fault profiles. The overall orientation of the faults within the failure region for basement-fault models with a convergent block-motion component (Figs. 11a–b) are roughly horizontal and terminate against the edges of regions of failure without propagating vertically very far into the layer. In contrast, in basement-fault models with a component of divergent block-motion, faults in the layer are more nearly vertically oriented and may propagate to significant vertical distances within the layer prior to intersecting the edge of the failure region. This suggests that for constant basement-fault displacement, not only will the region of failure be larger above normal faults than for reverse faults, but also faults associated with basement normal faults will be more efficient in propagating to the upper surface of the layer than will faults propagating above basement reverse faults.

DISCUSSION

The applicability of the results obtained from the present model to natural structures can be checked, in part, by comparing them with results obtained from laboratory models, such as those using rigid forcing blocks, that conform to the boundary conditions adopted in the mathematical models. Differences are to be expected, because the mathematical models only approximate the rheological behavior and boundary conditions of the experimental models, or those applying to natural structures. However, the comparison provides a guide to the sensitivity of modeled and natural features to those conditions. Application of results from either kind of model to natural structures will still depend on whether the model conditions conform to those in nature.

Deformation of the layer

The deformation of the layer in our models compares well with that observed in laboratory model studies (Fig. 1) despite significant differences between the rheological behavior of the materials. Malavieille (1984) generated one-sided, horizontal convergence at the base of a sand layer using a conveyor-like assembly in which the 'rigid block' carrying the sand is subducted beneath a second, stationary rigid block (Fig. 1a). The upward-widening anticline, centered above the point of convergence between the translating and fixed 'blocks' is equivalent to that produced in the present model (Fig. 7a). Similarly, one-sided horizontal divergence at the base of a clay layer (Cloos 1968) generates an upward-widening syncline, centered above the point of divergence (Fig. 1e) like that in the present model (Fig. 7e).

As noted in the Introduction, the set of basal boundary conditions (1a) and (3a), for purely horizontal block motion, are *nearly identical* to those imposed in the experiments of Cloos (1968) and Malavieille *et al.* (1993), both of which are meant to apply to situations involving an horizontal decollement, or detachment surface. In view of the importance of such experiments in current thinking in structural geology, we offer the following detailed comments.

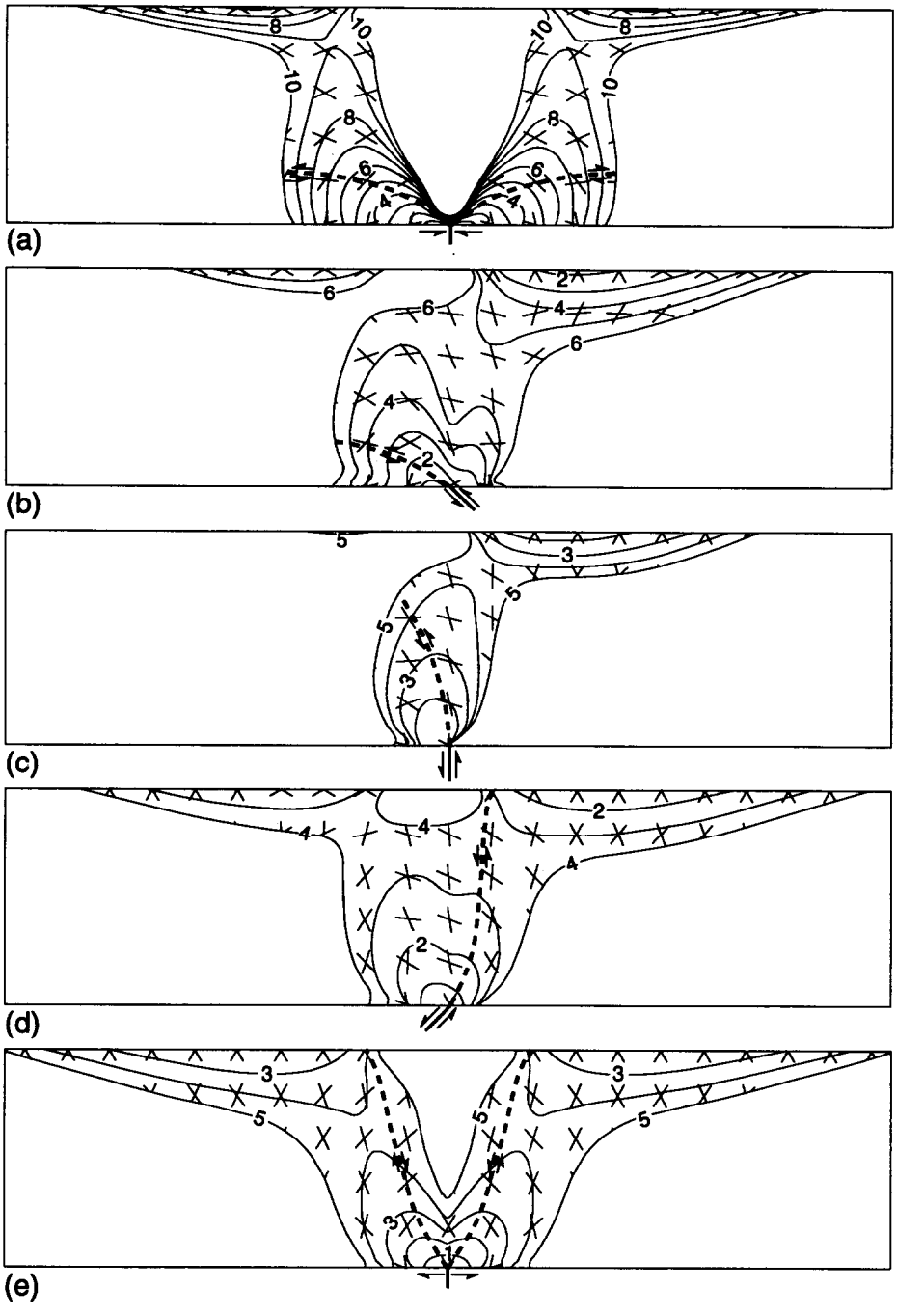

Fig. 11. Regions of potential failure associated with the layer, block-motion models of a: (a) convergent, horizontal fault; (b) reverse fault with 45° dip; (c) vertical fault; (d) normal fault with 45° dip; and (e) divergent, horizontal fault. Contours connect loci of failure for a given fault displacement (U) and the associated contour values correspond to the magnitude of the fault displacement. The highest contour in each diagram represents the basement-fault displacement necessary for loci of failure to cross the entire layer. Note that 10m of basement-fault displacement are required to accomplish complete failure of the layer in model (a), while only 5m of fault displacement are required in (c). Conjugate fault trajectories are indicated by 'X'. The acute angle of the 'X' is bisected by the principal compressive stress. The fault in the clockwise direction from the bisector has a left-lateral sense of slip while the fault in the counter-clockwise direction has a right-lateral sense of slip.

In one of his experiments, Cloos (1968) produced a structure in clay cake analogous to that seen above a listric normal fault by pulling on an inextensible metal sheet from beneath another, normal to the straight edge of the latter. Both sheets were supported by an horizontal surface, so that their relative motion was horizontal, and, hence, satisfied (3a). At its base, the clay cake adhered—for the most part—to the metal sheet underlying it, and, after some preliminary deformation, a normal fault formed between the edge of the upper, fixed, sheet and the surface of the layer. Indeed, 'nearly identical' may not be accepted by some readers as an accurate statement. One difference, perhaps not easily controlled by the experimentalist, has to do with the

deviation from perfect adherence between the clay cake, at its base, to one or the other metal sheet. It is clear that as one plate is pulled, new surface area will emerge from beneath the fixed plate, and that to this, the clay, at the base of the hanging wall along the newly-formed fault, will come to adhere to a greater or lesser extent.

The second difference, to which we attach the greater significance, can be stated in precise mathematical terms. To clearly present this, we shall describe a modified experimental set-up. Suppose the metal sheets used by Cloos are replaced by two inextensible, but flexible, sheets, composed, for example, of Mylar. Let the sheets be supported by a horizontal table. Instead of having the two sheets overlap, let them both be effectively unbounded, and both feed into a straight slot in the table. Then, either sheet may be independently pulled horizontally, from beyond the edges of the overlying clay cake, or, if desired, held fixed by being suitably clamped at both ends. The Cloos experiment corresponds to the case that one sheet is pulled, and the other is held fixed. The boundary condition (1a), with $\delta=0$, and $V>0$, corresponds to the case that both sheets are pulled with the same speed. The boundary condition corresponding to the Cloos experiment is achieved by replacing (1a) by

$$u(x,0)=\begin{cases}-V\cos\delta - V\cos\delta & -L/2\le x\le 0\\ +V\cos\delta - V\cos\delta & 0\le x\le L/2\end{cases} \quad (6)$$

In this case, the velocity at the base of the material to the right of the origin, $x = 0$, is zero. The speed of the sheet on the left of the origin is twice that in the previous case, but the relative motion, between sheets, is the same.

Cloos (1968) also performed an experiment which initially corresponded to the boundary condition (1a). Interestingly, he did this by resting a clay cake on two boards, i.e. rigid blocks, in contact, and pulling them apart. Because the part of the clay cake between the separating boards becomes unsupported, or, if one used sheets of metal initially in contact, but resting on a table, part of the clay cake does not adhere to a moving plate, the experiment does not continue to correspond to the condition (1a). The alternate experiment described will, provided the clay continues to adhere to the new surface area of the sheets.

Now, if the material comprising the clay cake maintained its initial, uniform, properties throughout the experiment—which it does not, since a well-defined fault surface develops, if a condition of adherence were strictly satisfied, and if the layer thickness were maintained constant, by the addition of new material to the region in which thinning is occurring, then the following would be true. The distribution of stress and of the rate of deformation would be identical in the two experiments—that in which one sheet alone were pulled, and that in which both sheets were pulled at equal speeds. The velocity field would differ only in terms of a uniform translation to the left, in the first experiment, as we have described it. As a consequence of the last, the distribution of strain and the form of deformed marker horizons would be different: these would be asymmetric in the first experiment, and symmetric in the second.

In the case of the present model, the clay cake is replaced by a Newtonian viscous layer, and what has been just said applies in detail. We have, in fact, worked up the equivalents of the two experiments for a large finite deformation. Evidently, no faults nor fault-like features can occur in the fluid layer, so the results are different in this respect from the Cloos experiment. Such results could be readily duplicated by means of the methodology presented in this paper.

Returning to the description of the experiments in terms of the pulling or fixing of Mylar sheets, if one, or both of the sheets are pulled into the slot, analogous, compressional structures will be produced. We would identify these types of structures with the models of Malavieille (1984) and Malavieille *et al.* (1993), and others.

With regard to the application of these models to structures formed above detachment surfaces, we may make the following remarks. Mylar sheets, metal plates, or inextensible sheets of any sort are not present at detachment surfaces in nature. The experimental models impose a boundary condition—that on the uniformity of the detachment-parallel velocity, that is not a natural condition to impose at a detachment surface. A natural condition might, for example, relate the slip rate on the detachment surface to the normal and shear tractions. In the case of material possessing finite strength, as in the case of a clay cake, the velocity field arising in a natural or experimental deformation may possess the property stipulated in these models. In the case of fluid-like behavior, they will not.

Rock-laminate experiments modeling reverse (Figs. 1b and 12a), vertical (Fig. 12b) and normal basement-fault (Fig. 12c) motions, show upward-widening monoclines. The location of the limb of the monocline, relative to the location of the basement fault, is dependent upon the basement-fault dip and sense of slip. For a reverse basement fault, the limb lies to the west of the fault tip. For vertical and normal basement-fault models, the limb lies directly above and to the east of the basement fault, respectively. In a series of experiments in mixed sand and clay modeling dipping basement faults (Tsuneishi 1978), the same relationship between the location of the 'flexure zone' and the attitude and sense of slip of the basement fault is observed.

The low-amplitude anticline and syncline superposed on a monocline which appears in the block-motion model (Figs. 7b & d), is observed when a clay layer is deformed above a basement fault. Withjack *et al.* (1990) show a subtle syncline on the downthrown limb of a monocline generated above a basement normal fault, with 45° dip. A syncline is not seen in experiments with 60° and 75° basement normal faults. Similarly, our block-motion model of a basement normal fault with dip in excess of 45° shows reduced expression of the syncline as the basement-fault angle approaches 90°. Rodgers & Rizer (1981) show an experimental model of a clay-cake

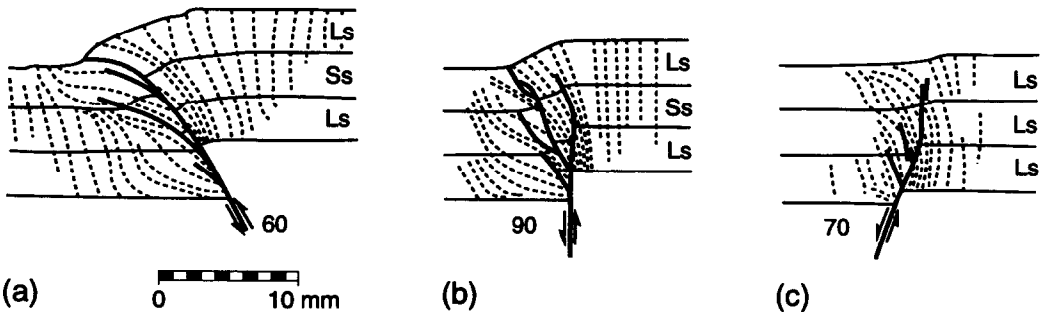

Fig. 12. Faults (heavy lines) and inferred, maximum-compressive stress trajectories (dashed lines) in multilayer experiments, with limestone (Ls) and sandstone (Ss) rock-beams. The experiments were run at 100 MPa confining pressure and include, (a) a reverse basement fault dipping 60° (Friedman *et al.*, 1976a), (b) a vertical basement fault (Logan *et al.*, 1978), and (c) a normal basement fault dipping 70° (Patton 1984).

deformed above a basement reverse fault. An internal marker and the upper surface of the clay-cake takes the form of a low-relief anticline superposed on the upper limb of the monocline, in agreement with the block-motion model.

The spatial and geometric dependence of monoclines on basement-fault dip and sense of slip, documented in both experimental and mathematical modeling studies, may permit estimates of the position of a buried fault beneath a monocline, and its dip and sense of slip. Brock & Nicolaysen (1975, Fig. 8) have interpreted the Brady Unit monocline in the Wyoming foreland to be underlain by a vertical basement fault. However, the position of the monoclinal limb relative to the location of the basement fault would argue for a basement reverse-fault interpretation. However, as demonstrated by Reches (1978) and Reches & Johnson (1978), such monocline–fault relationships can be very sensitive to the stratigraphy of the monocline and the boundary conditions, making unequivocal interpretations difficult.

Stress state of the layer

Information on the stress distribution in experimental and natural structures is difficult to obtain. Experiments which allow for the extraction of stress-state information are photoelastic models (e.g. Rodgers & Rizer 1981, Wiltschko & Eastman 1988) and structures generated with rock laminates above rigid blocks.

Good agreement is obtained between the orientation of maximum compressive stress derived from the mathematical block-motion models and that inferred from calcite twin lamellae and microcracks in constituent grains of small-displacement rock models (Fig. 12) for reverse- (Friedman *et al.*, 1976a, Gangi *et al.*, 1977), vertical- (Logan *et al.*, 1978) and normal-fault (Patton 1984) block-motion. In the region vertically above the fault, both mathematical (Figs. 10b–d) and experimental (Fig. 12) models show compressive stress trajectories that are arcuate and concave towards the downthrown side of the basement fault. Arcuate stress trajectories are present well into the upper reaches of the rock layers, west of the induced fault system in the rock layers, where they have attitudes which are nearly horizontal for reverse basement-fault models (Fig. 12a), and inclined at 45° for vertical and normal basement-fault rock models (Figs. 12b–c), as in the mathematical block-motion models (Fig. 10). Both experimental and mathematical models have nearly horizontal trajectories immediately to the west of the basement-fault location at the base of the layer. The reverse basement-fault model shows the most areally extensive expression of horizontal trajectories, and the normal-fault model shows the least. The vertical stress trajectories to the west of the vertical fault (Fig. 12b), and to the east and west of the reverse fault (Fig. 12a), in the rock models are at 90° to those found in the mathematical models (Figs. 10b–c). This inconsistency most likely reflects an aspect of the experimental conditions not accounted for in the boundary conditions of our models. However, the mathematical models suggest that the maximum shear stress is low in these regions (Figs. 9b–d) and its effects would not likely be seen in the rock models. Furthermore, the basement faults at the base of the rock models in Fig. 12 have experienced significant displacement relative to the dimensions of the layers, and the layers are composed of rock laminates. Ideally, stress-state comparisons between our model and experimental block-motion models need to be made with single-layer, isotropic rock layers deformed at small displacements.

Reches (1978) analyzed paleostress indicators across the Palisades monocline in Arizona. The monocline is a gentle fold above a subvertical basement fault. Reches (1978) documented layer-parallel, maximum compressive stress orientations on both the upthrown and downthrown sides of the fault. This contrasts with the arcuate trajectory patterns in the vertical, block-motion model (e.g. Fig. 10c), which record the transition from vertical maximum compressive stress orientations on the upthrown side of the basement fault to horizontal orientations on the downthrown side. However, Reches (1978) found that the compressive stress state documented in profile was related to a regional, subhorizontal compression which was present during the time of monocline development.

The Casper Mountain structure in the Wyoming Foreland is a monocline above a basement reverse fault (Narr & Suppe 1989). In their study of paleostress orientations of cover rocks at Casper Mountain, Narr & Suppe (1989) recorded, in the lower limb of the monocline near the tip

of the basement fault, maximum and minimum compressive stress orientations which are approximately horizontal and vertical, respectively. The orientations change by 90° in the upper limb of the monocline as do the orientations in the block-motion models. Narr & Suppe (1989) attribute the change in stress orientation at Casper Mountain to bending, an explanation which is supported by the mathematical, block-motion models.

Brittle failure of the layer

Initial failure of a sand or clay layer with horizontal convergent block motion (Malavieille 1984) and horizontal divergent block motion (Cloos 1968) produces a symmetric array of faults about the point of block interaction (Figs. 1a & e). The faults dip toward the basement-fault location and are reverse for the convergent model and normal for the divergent model, comparing well with faults inferred from the stress distributions obtained from the block-motion models (Figs. 11a & e).

In experimental models of reverse (Friedman *et al.*, 1976a, 1980, Couples & Stearns 1978, Tsuneishi 1978), vertical (Sanford 1959, Lowell 1970, Horsfield 1977, Stearns *et al.*, 1978, Logan *et al.*, 1978, Tsuneishi 1978) and normal (Horsfield 1977, Tsuneishi 1978, Patton 1984, Withjack *et al.*, 1990) basement faults, arrays of arcuate, concave-downward faults converge downward to the location of the basement fault (Figs. 1b–d and 12). Again, the arcuate fault traces in the experimental models correlate well with those inferred from the mathematical models (Fig. 11). Arcuate faults are also inferred in other mathematical treatments (e.g. Sanford 1959, Gangi *et al.*, 1977, Couples 1977, Rodgers & Rizer 1981).

When sequential development of faults is observed in experimental models, with increasing basement-fault displacement, the propagation of the earliest, deepest, fault is arrested before it reaches the upper surface of the layer (Sandford 1959, Stearns 1978, Logan *et al.*, 1978, Friedman *et al.*, 1976a, Patton 1984, Withjack *et al.*, 1990). This fault then becomes inactive, and younger faults form behind, and toward the upthrown side of the earlier faults. The later faults may also be abandoned. This sequential propagation and abandonment of arcuate faults results in a nested array of abandoned faults commonly preserved in the downthrown fault block. The intersection of arcuate faults, emanating from near the tip of the basement fault, with the boundary of the area of failure, provides a mechanism for forming abandoned arcuate faults. The sequence of abandoned arcuate faults suggests that the stress distribution is not greatly altered during the development of a through-going fault system. In further support of this idea, finite-element models (Jamison 1979, Stein & Wickham 1980) for large displacement on an upward-propagating fault also demonstrate persistent, arcuate, concave-downward principal stress orientations in deforming beams. The analogy with the self-similar stress pattern for a crack propagating in an unbounded region comes to mind; the presence of a free surface would result in a change in stress distribution away from the crack tip and in the stress intensity factor as a crack propagated towards it. Hence, the present mathematical models may simulate both the state of stress at initial failure, and, to a rougher approximation, that prior to the establishment of a through-going fault.

As discussed previously, the model results suggest that (Fig. 11) a layer deformed above a basement normal fault will tend to fail at a smaller displacement than one deformed by a basement reverse fault. Experimental support for this is provided by rock laminate models (Friedman *et al.*, 1976a, Logan *et al.*, 1978, Patton 1984) deformed at constant confining pressure. The models in Fig. 12 have been deformed just to the point where the induced faults have intersected (Fig. 12a) or are about to intersect (Figs. 12b–c) the upper surface of the upper rock layer. Note that when the experiments reach this stage of development, the basement-fault displacement is the least for the normal-fault model, intermediate for the vertical-fault model, and greatest for the reverse-fault model.

Acknowledgements—Initial development of the mathematical model for this study was partially funded under National Science Foundation Grant #EAR77-13097, M. Friedman (P.I.). We gratefully acknowledge reviews of earlier versions of this manuscript by Richard Gibson, Jean-Pierre Petit, Jean-Pierre Brun and an anonymous reviewer. We thank Dave Stearns, John Logan and Mel Friedman for numerous stimulating discussions and ideas which aided in the development and understanding of these models.

REFERENCES

Brock, W. G. & Nicolaysen, J. 1975. Geology of the Brady Unit, Sweetwater County, Wyoming. In: *Deep Drilling Frontiers of the Central Rocky Mountains* (Edited by Bolyard, D. W.). Rocky Mountain Association of Geologists—1975 Symposium, pp. 225–237.

Cloos, E. 1968. Experimental analysis of Gulf Coast fracture patterns. *Bull. Am. Ass. Petrol. Geol.* **52**, 420–444.

Couples, G. 1978. Comments on applications of boundary-value analyses of structures of the Rocky Mountains foreland. In: Laramide folding associated with basement block faulting in the Western United States (Edited by Matthews, V. III.). *Mem. geol. Soc. Am.* **151**, 197–214.

Couples, G. 1977. Stress and shear fracture (fault) trajectories resulting from a suite of complicated boundary conditions with applications to the Wind River Mountains. *Pure & Appl. Geophys.* **115**, 113–133.

Couples, G. & Stearns, D. W. 1978. Analytic solutions applied to structures of the Rocky Mountains foreland on local and regional scales. In: Laramide folding associated with basement block faulting in the Western United States (Edited by Matthews, V. III.). *Mem. geol. Soc. Am.* **151**, 313–335.

Friedman, M., Handin, J., Logan, J. M., Min, K. D. & Stearns, D. W. 1976a. Experimental folding of rocks under confining pressure: part III. Faulted drape folds in multilithologic layered specimens. *Bull. geol. Soc. Am.* **87**, 1049–1066.

Friedman, M., Teufel, L. W. & Morse, J. D. 1976b. Strain and stress analyses from calcite twin lamellae in experimental buckles and faulted drape-folds. *Phil. Trans. R. Soc.* **283**, 87–107.

Friedman, M., Hugman, R. H. H., III & Handin, J. 1980. Experimental folding of rocks under confining pressure, part VIII—forced folding of unconsolidated sand and of lubricated layers of limestone and sandstone. *Bull. geol. Soc. Am.* **91**, 307–312.

Gangi, A. F., Min, K. D. & Logan, J. M. 1977. Experimental folding of rocks under confining pressure: part IV—theoretical analysis of faulted drape-folds. *Tectonophysics* **42**, 227–260.

Hafner, W. 1951. Stress distribution and faulting. *Bull. geol. Soc. Am.* **62**, 1–28.
Haneberg, W. C. 1992. Drape folding of compressible elastic layers—I. Analytical solutions for vertical uplift. *J. Struct. Geol.* **14**, 713–721.
Haneberg, W. C. 1993. Drape folding of compressible elastic layers—II. Matrix solution for two-layer folds. *J. Struct. Geol.* **15**, 923–932.
Horsfield, W. T. 1977. An experimental approach to basement-controlled faulting. *Geologie Mijno.* **56**, 363–370.
Howard, J. H. 1966. Structural development of the Williams Range thrust, Colorado. *Bull. geol. Soc. Am.* **77**, 1247–1264.
Jamison, W. R. 1979. Laramide Deformation of the Windgate Sandstone, Colorado National Monument: A Study of Cataclastic Flow. Ph.D. Thesis, Texas A&M University, College Station, Texas.
Kilsdonk, B. & Fletcher, R. C. 1989. An analytic model of hanging-wall and footwall deformation at ramps on normal and thrust faults. *Tectonophysics* **163**, 153–168.
Lanczos, C. 1961. *Applied Analysis*. Prentice Hall, Englewood Cliffs N.J.
Logan, J. L., Friedman, M. & Stearns, M. T. 1978. Experimental folding of rocks under confining pressure: Part VI. Further studies of faulted drape folds. In: Laramide folding associated with basement block faulting in the Western United States (Edited by Matthews, V. III.). *Mem. geol. Soc. Am.* **151**, 235–271.
Lowell, J. D. 1970. Antithetic faulting in upthrusting. *Bull. Am. Ass. Petrol. Geol.* **54**, 1946–1950.
Malavieille, J. 1984. Modélisation expérimentale des chevauchements imbriqués: application aux chaînes de montagnes. *Bull. Soc. géol. Fr.* **26** *Ser.* 129–138.
Malavieille, J., Larroque, C. & Classou, S. 1993. Modélisation expérimentale des relations tectonique/sédimentation entre bassin avant-arc et prisme d'accrétion. *C. r. hebd: Acad. Séanc. Sci. Paris* **316**, 1131–1137.
Narr, W. & Suppe, J. 1989. Basement deformation in low-temperature, basement-involved, compressive structures (ms): Department of Geological and Geophysical Sciences, Princeton University, 25.
Patton, T. L. 1984. Normal-fault and Fold Development in Sedimentary Rocks above a Pre-existing Basement Normal Fault. Ph.D. Thesis, Texas A&M University, College Station, Texas.
Reches, Z. 1978. Development of monoclines: Part I. Structure of the Palisades Creek branch of the East Kaibab monocline, Grand Canyon, Arizona. *Mem. geol. Soc. Am.* **151**, 235–271.
Reches, Z. & Johnson, A. M. 1978. Development of monoclines: Part II. Theoretical analysis of monoclines. In: Laramide folding associated with basement block faulting in the Western United States (Edited by Matthews, V. III.). *Mem. geol. Soc. Am.* **151**, 273–311.
Rodgers, D. A. & Rizer, W. D. 1981. Deformation and secondary faulting near the leading edge of a thrust fault. In: Thrust and nappe tectonics (Edited by McClay, K. R. & Price, N. J.). *Spec. Publs. geol. Soc. Lond.* **9**, 65–77.
Sanford, A. R. 1959. Analytical and experimental study of simple geologic structures. *Bull. geol. Soc. Am.* **70**, 19–52.
Stearns, D. W. 1978. Faulting and forced folding in the Rocky Mountains foreland. In: Laramide folding associated with basement block faulting in the Western United States (Edited by Matthews, V. III.). *Mem. geol. Soc. Am.* **151**, 1–37.
Stearns, D. W. & Weinberg, D. M. 1975. A comparison of experimentally created and naturally formed drape folds. *Twenty-seventh Annual Field Conference—1975, Wyoming Geological Association Guidebook*, pp. 159–166.
Stearns, D. W., Couples, G. & Stearns, M. T. 1978. Deformation of nonlayered materials that affect structures in layered rocks. *Thirteenth annual field conference—1978, Wyoming Geological Association Guidebook*, pp. 213–225.
Stein, R. & Wickham, J. 1980. Viscosity-based numerical model for fault-zone development in drape folding. *Tectonophysics* **66**, 225–251.
Tsuneishi, Y. 1978. Geological and experimental studies on mechanism of block faulting. *Bulletin of the Earthquake Research Institute* (Japan) **53**, 173–242.
Weinberg, D. M. 1979. Experimental folding of rocks under confining pressure: Part VII. Partially scaled models of drape folds. *Tectonophysics* **54**, 1–24.
Wiltschko, D. V. & Eastman, D. B. 1988. A photoelastic study of the effects of preexisting reverse faults in basement on the subsequent deformation of the cover. *Mem. geol. Soc. Am.* **171**, 111–118.
Withjack, M. O., Olson, J. & Peterson, E. 1990. Experimental models of extensional forced folds. *Bull. Am. Ass. Petrol. Geol.* **74**, 1038–1054.

APPENDIX

The solution for the stress and velocity distributions in a layer overlying a periodic sequence of faults with dip, δ, relative rate of slip, V, and alternating sense of slip, is obtained by summing expressions for two component solutions, one for purely vertical block motions, and one for purely horizontal motions (separation or 'inter-penetration'). For the vertical block motions, the horizontal and vertical velocity components at the base of the layer are given by (1b) and (3b). The form of the vertical velocity component in (1b) can be approximated by the truncated series

$$w(x,0) = \sum_{n=1}^{N} V_n \sin(n\lambda x) \tag{A1}$$

where $\lambda = 2\pi/L$,

$$V_n = V \sin\delta\,(4/n\pi)\Gamma_n \qquad n = 1, 3, 5, \ldots$$

the terms with even n vanishing, and

$$\Gamma_n = \sin[n\pi/(N+1)]/[n\pi/(N+1)]$$

is the Gibbs' factor (Lanczos, 1961), which improves the smoothness and convergence properties of the series.

For the horizontal block motions, the velocity components at the base of the layer are (1a) and (3a). The horizontal component will likewise be represented by the truncated series

$$u(x,0) = \sum_{n=1}^{N} V_n' \sin(n\lambda x) \tag{A2}$$

where

$$V_n' = V \cos\delta\,(4/n\pi)\Gamma_n \qquad n = 1, 3, 5, \ldots$$

In either case, at the horizontal surface of the layer, $z = H$, the normal and shear tractions vanish, yielding the condition (2).

For vertical block motion, the solution can be written in terms of a stress function

$$\phi^{(v)}(x,z) = -2\eta \sum_{n=1}^{N} [1/(n\lambda)]\{[A_n + B_n(n\lambda z - 1)]e^{n\lambda z} + [C_n + D_n(n\lambda z + 1)]e^{-n\lambda z}\}\cos(n\lambda x) \tag{A3}$$

where

$$\sigma_{xx} = \partial^2\phi/\partial z^2$$
$$\sigma_{zz} = \partial^2\phi/\partial x^2$$
$$\sigma_{xx} = -\partial^2\phi/\partial x\partial z \tag{A4}$$

or a stream function

$$\Psi^{(v)}(x,z) = +\sum_{n=1}^{N} [1/(n\lambda)]\{[A_n + B_n(n\lambda z - 1)]e^{n\lambda z} - [C_n + D_n(n\lambda z + 1)]e^{-n\lambda z}\}\cos(n\lambda x) \tag{A5}$$

where

$$u = \partial\Psi/\partial z$$
$$w = -\partial\Psi/\partial x \tag{A6}$$

Application of the boundary conditions yields four relations determining the arbitrary coefficients A_n, B_n, C_n, and D_n

$$A_n + B_n = 0$$
$$A_n - B_n - C_n - D_n = V_n$$
$$[A_n + B_n(n\lambda H - 1)]e^{n\lambda H} + [C_n + D_n(n\lambda H + 1)]e^{-n\lambda H} = 0$$
$$[A_n + B_n(n\lambda H)]e^{n\lambda H} - [C_n + D_n(n\lambda H)]e^{-n\lambda H} = 0 \tag{A7}$$

For the horizontal block motion, the stress function is

$$\phi^{(h)}(x,z) = -2\eta \sum_{n=1}^{N} [1/(n\lambda)]\{[A_n' + B_n'(n\lambda z - 1)]e^{n\lambda z} + [C_n' + D_n'(n\lambda z + 1)]e^{-n\lambda z}\}\cos(n\lambda x) \tag{A8}$$

and the stream function is

$$\Psi^{(h)}(x,z) = -\sum_{n=1}^{N} [1/(n\lambda)]\{[A'_n + B'_n(n\lambda z - 1)]e^{n\lambda z} - [C'_n + D'_n(n\lambda z + 1)]e^{-n\lambda z}\} \sin(n\lambda z) \quad \text{(A9)}$$

The first pair of relations in (A7) are replaced by

$$A'_n + B'_n = -V'_n$$
$$A'_n - B'_n - C'_n - D'_n = 0 \quad \text{(A10)}$$

and the second pair remain the same, except that A_n is replaced by A'_n, and so forth.